Earth and Planetary Science Letters 367 (2013) 82–94

Contents lists available at SciVerse ScienceDirect

Earth and Planetary Science Letters

journal homepage: www.elsevier.com/locate/epsl

Subduction of oceanic asthenosphere: A critical appraisal in central Alaska

Teh-Ru Alex Song [a,*], Hitoshi Kawakatsu [b]

[a] Institute for Research on Earth Evolution, Japan Agency for Marine-Earth Science and Technology Center, 3173-25 Showa-Machi, Yokohama 237-0005, Japan
[b] Earthquake Research Institute, the University of Tokyo, 1-1-1 Yayoi, Bunkyo-ku, Tokyo 113-0032, Japan

ARTICLE INFO

Article history:
Received 21 September 2012
Received in revised form
9 February 2013
Accepted 12 February 2013
Editor: P. Shearer

Keywords:
oceanic asthenosphere
subduction
sub-slab seismic anisotropy
radial anisotropy
shear-wave splitting
Alaska

ABSTRACT

Song and Kawakatsu (2012) have shown that the sub-slab fast splitting pattern observed in most subduction zones can be a direct consequence of subduction of the oceanic asthenosphere that has strong radial anisotropy. This model not only explains the non-intuitive trench-parallel splitting pattern in most of subduction zones, but also predicts the trench-normal behavior (fast polarization direction sub-parallel to the absolute plate motion of the incoming plate) observed in several shallow subduction zones. The general validity of such a scenario is crucial to fundamental understandings of the development of mantle anisotropy in sub-lithosphere or/and sub-slab conditions, the nature and formation of oceanic asthenosphere as well as the flow pattern and mass transport near subduction zones. To validate this scenario, we examine SKS splitting patterns observed across the fore-arc in central Alaska. Here the fast splitting direction varies from plate motion sub-parallel near the trench to mostly trench-parallel beyond the 100 km slab-isodepth contour, while being strongly variable in between. After taking into account the rotation of anisotropy symmetry in the oceanic asthenosphere with respect to the local plate motion obliquity and down-dip variations in the slab dip, we reproduce a general 90-degree switch in fast splitting direction as well as the back azimuth dependent splitting pattern across the entire fore-arc. The current validation further augments the idea that, apart from anisotropy in the mantle wedge and the subducting slab, subduction of the oceanic asthenosphere is likely to be the dominant source of seismic anisotropy in central Alaska and potentially in many subduction zones. Furthermore, this result also provides alternative views to models of seismic anisotropy in the mantle wedge and on the length scale in which the 3D mantle flow may be important.

1. Introduction

Seismic anisotropy has been widely used to infer patterns of mantle flow in various tectonic environments and these efforts have led to a better understanding of the style of deformation and the rheology that are relevant to plate tectonics (Ando et al., 1983; Silver, 1996; Savage, 1999; Fouch and Rondenay, 2006). While the subduction zone is one of the centerpieces in plate tectonics, the mantle flow around the slab has been of great interest and frequently inferred from seismic anisotropy through the analysis of shear wave birefringence, or shear-wave splitting (Vinnik et al., 1984; Silver, 1996; Savage, 1999). Previously, Russo and Silver (1994) and Long and Silver (2008, 2009) showed that sub-slab shear wave fast splitting directions are generally parallel or sub-parallel to the trench in most subduction zones, which is in conflict with the prediction of trench-normal fast splitting direction based upon the classical slab entrained flow with the A-type olivine fabric (Mainprice and Silver, 1993; Ismail and Mainprice, 1998; Karato et al., 2008). Consequently, the hypothesis of trench-parallel flow beneath the subducting slab has been proposed to explain these observations. While several alternative hypotheses exist, such as hydrated faulting (Faccenda et al., 2008) within the slab and a change of olivine slip system (Jung et al., 2009), we focus our discussion on the flow direction coupled with the effect of the anisotropy symmetry and the subduction geometry.

One of the missing ingredients not taken into account in forming previous hypotheses is that the anisotropic fabric of the oceanic asthenosphere beneath oceanic basins prior to subduction indicates strong radial anisotropy (e.g., Montagner and Tanimoto, 1991; Gung et al., 2003; Panning and Romanowicz, 2006; Nettles and Dziewonski, 2008; Kustowski et al., 2008; Lekic and Romanowize, 2011), as well as relatively weak azimuthal anisotropy (e.g., Smith et al., 2004; Debayle et al., 2005; Maggi et al., 2006) comprising an effective orthorhombic symmetry. Such an orthorhombic symmetry in the oceanic asthenosphere differs from the typical A-type olivine fabric, which instead shows a much stronger azimuthal anisotropy than radial anisotropy (e.g., Mainprice, 2007; Karato et al., 2008). Indeed, some of the recent models of the oceanic asthenosphere invoke the idea that radial anisotropy is a characteristic property of the asthenosphere (Kawakatsu et al., 2009; Holtzman and Kendall, 2010).

* Corresponding author. Tel.: +81 80 4154 0617; fax: +81 45 778 5498.
E-mail address: tehrusong@gmail.com (T.-R. Song).

0012-821X/$ - see front matter © 2013 Elsevier B.V. All rights reserved.
http://dx.doi.org/10.1016/j.epsl.2013.02.010

With these in mind, Song and Kawakatsu (2012) demonstrated the importance of the anisotropy symmetry on the shear wave splitting pattern with respect to the incident angle of the incoming wave and the slab geometry. Assuming that the oceanic asthenosphere subducts along with the slab, they constructed an elastic tensor that is representative of effective orthorhombic anisotropy in the oceanic asthenosphere, and rotated symmetry axes with respect to the slab dip. They demonstrated that such a model can simultaneously explain the sub-slab trench-parallel splitting pattern observed globally (Long and Silver, 2008, 2009) as well as several apparent exceptions in shallow subduction zones such as Cascadia (Currie et al., 2004) and Alaska (Christensen and Abers, 2010; Hanna and Long, 2012), which display the fast splitting direction sub-parallel to the plate motion direction at stations near the trench.

While subduction of the oceanic asthenosphere appears capable of explaining gross features of SKS splitting observations in subduction zones globally, it is important to verify such a scenario through a more strict test by examining how SKS splitting observations vary with the ray back azimuth in a single subduction zone where the slab dip also varies with depth. In this article, we examine SKS splitting observations in central Alaska where Christensen and Abers (2010) and Hanna and Long (2012) provide high quality measurements at different back azimuths across the entire fore-arc (Fig. 1, Supplementary Fig. S1). In addition, the slab dip beneath central Alaska changes from about 5° near the trench to beyond 30°–35° beneath the deep wedge (Fig. 2, Supplementary Fig. S2). This provides an excellent opportunity to examine our scenario of a subducting oceanic asthenosphere and to critically evaluate how the tilted anisotropy symmetry in the subducted oceanic asthenosphere modulates the splitting pattern through the slab dip change. Although local S wave splitting measurements are not available in the literature, this SKS splitting dataset will prove to be crucial in understanding how the slab geometry modulates the observed splitting pattern across the fore-arc and in distinguishing the scenario of the subduction of the asthenosphere from other hypotheses.

We refer to the term “subduction of oceanic asthenosphere” as a slightly different expression from the slab entrainment to emphasize on a model where the entrained sub-slab mantle displays an anisotropy property analogous to that of the oceanic asthenosphere beneath ocean basins except that the angle of symmetry axis changes with the slab dip. We will alternatively use the term “subducting asthenosphere” or “subduction of oceanic asthenosphere” in the rest of the article to discuss our model prediction along with other hypothesis. In the following sections, we will first detail the slab geometry, observed splitting pattern and the procedures of our forward modeling approach.

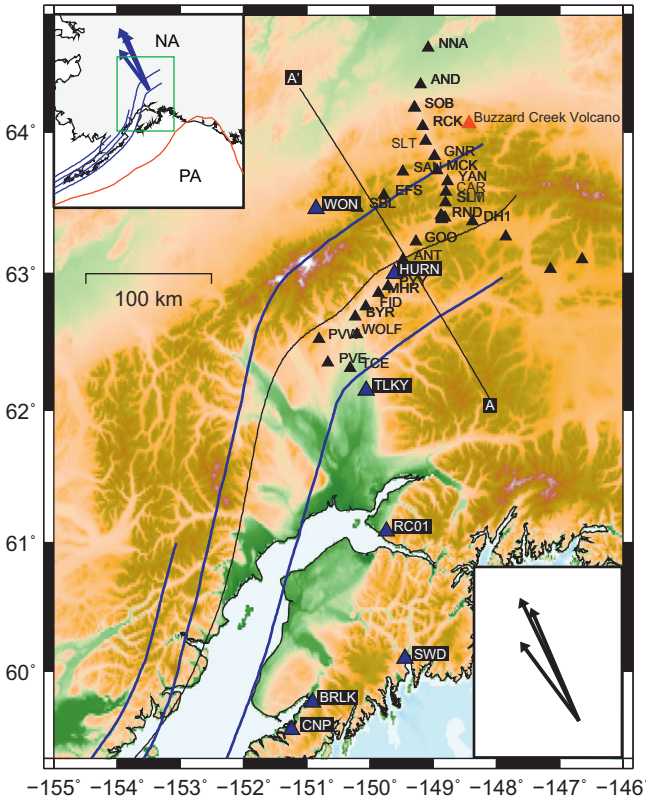

Fig. 1. Tectonic map of central Alaska region. Slab contours of 50, 100 and 150 km isodepths follow Ratchkovski and Hansen (2002). USGS slab contour of 100 km (Hayes et al., 2012) is also shown to indicate possible variations in slab strike (black line). Arrows in the lower-right panel indicate predicted absolute plate motion from NUVEL-1A (DeMets et al., 1994) for two Pacific hotspot reference frames HS3 (Gripp and Gordon, 2002) and HS2 (Gripp and Gordon, 1990), and one Atlantic hotspot reference frame (Kreemer, 2009). Seismic stations from BEEAR experiment and a few stations of the Alaska network are shown by solid triangles. The Buzzard Creek Volcano in the northeast corner of the BEEAR experiment is shown in red triangle. Upperleft inset displays a large scale tectonic framework where the Pacific plate (PA) subducts beneath the North America plate (NA). Back azimuthal variations in observed SKS splitting patterns can be referred to Supplementary Fig. S1. (For interpretation of the references to color in this figure legend, the reader is referred to the web version of this article.)

2. Slab geometry and SKS splitting patterns across the fore-arc central Alaska

We focus on SKS splitting observations by Christensen and Abers (2010) and Hanna and Long (2012) in central Alaska, more precisely near the Mckinley block, where the slab geometry is relatively well defined. The slab strike changes abruptly in the west and the inferred eastern edge is located at a few hundred kilometers away in eastern Alaska (e.g., Ratchkovski and Hansen, 2002; Rossi et al., 2006; Eberhart-Phillips et al., 2006; Jadamec and Billen, 2010). The slab dip is well constrained by regional relocated seismicity (Ratchkovski and Hansen, 2002), receiver function studies (Ferris et al., 2003; Ai et al., 2005; Abers et al., 2006; Rossi et al., 2006; Rondenay et al., 2008, 2010; Kim et al., 2012), and seismic tomography (Zhao et al., 1995; Eberhart-Phillips et al., 2006) (see also Fig. 2). In detail, the slab is initially dipping at about 5° near the trench and up to 10°–15° at the 50 km isodepth contour (Abers et al., 2006; Kim et al., 2012). Subsequently, the dip increases to about 20°–25° between 50 and 120 km isodepth contours below the wedge corner (Ferris et al., 2003; Rossi et al., 2006; Eberhart-Phillips et al., 2006; Rondenay et al., 2008, 2010) before reaching 30°–35° or more further north beneath the deep wedge (Ratchkovski and Hansen, 2002; Abers et al., 2006; Rossi et al., 2006; Eberhart-Phillips et al., 2006). Beneath the deep wedge, the estimate of slab dip can range from 30°–35° (Abers et al., 2006, see also Fig. 2) to 40°–45° or more (Ratchkovski and Hansen, 2002; Rossi et al., 2006, see also Fig. 2a; Supplementary Fig. S2).

The reported splitting analyses (BEAAR for Christensen and Abers (2010) and the Alaska broadband seismic network for Hanna and Long (2012)) complement each other in spatial sampling (see also Fig. 3). Splitting data reported by Christensen and Abers (2010) mostly sample the mantle beyond the 50 km isodepth contour except the station TLKY, while the measurements made by Hanna and Long (2012) extend the sampling toward the trench near Kenai Peninsula, including measurements at Alaska broadband stations BRLK, CNP, RC01, and SWD. Measurements near the inferred slab edge in eastern Alaska are

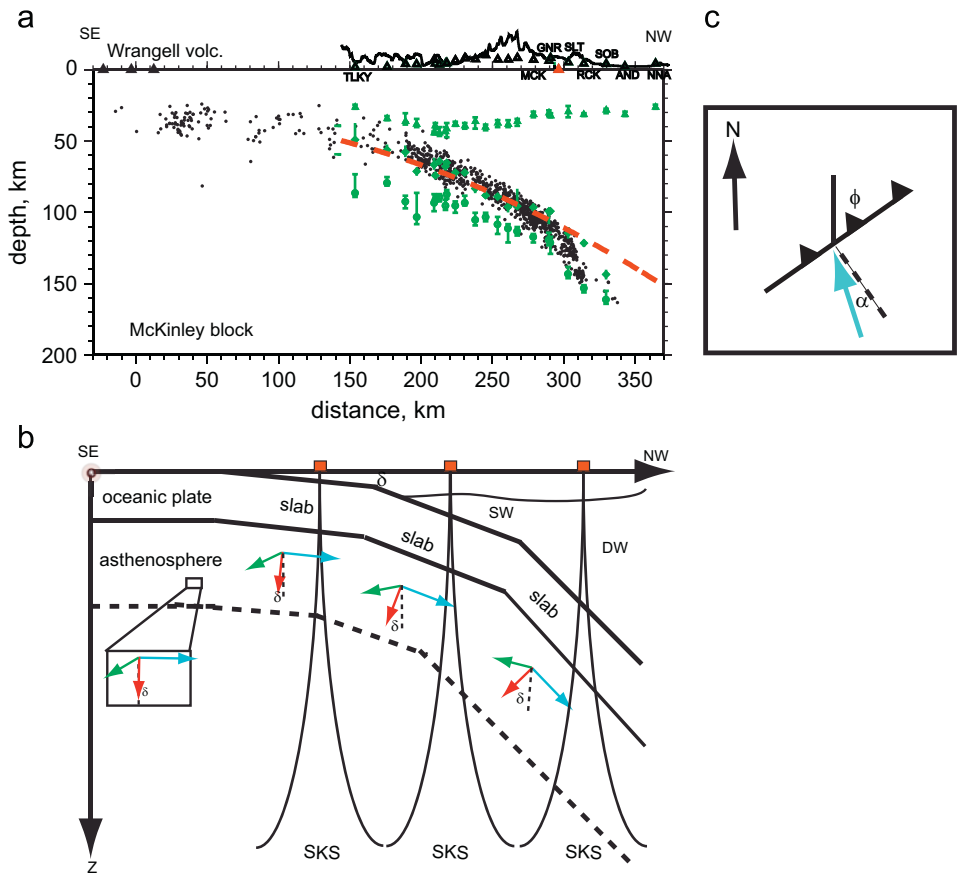

Fig. 2. Schematic diagram of slab geometry beneath central Alaska. (a) slab geometry delineated by seismicity profile C6 (Ratchkovski and Hansen, 2002), the polynomial fit of Abers et al. (2006) (red dashed line) and receiver function result of Rossi et al., (2006) (green diamonds and circles). The Buzzard Creek Volcano is indicated by red triangle. While seismicity profile C6 adapted here is more appropriate for most of the stations in the northeastern part of the array, the southwestern part of the array (from stations TLKY to HURN approximately, and station WON) is directly above the seismicity profile C5 of Ratchkovski and Hansen (2002), which is shown in Supplementary Fig. S2. Receiver function result of Rossi et al. (2006) also indicates a steepening in slab dip near station SLT and beyond ($>40^\circ$). (b). model configuration with the anisotropy symmetry in the oceanic asthenosphere rotating with respect to slab dip δ in different down-dip segments. The plate motion obliquity α is defined clockwise from trench-normal, shown in (c). The rotated elastic tensor is further rotated with respect to the strike of the trench (or slab contour), ϕ, defined clockwise from the north. (For interpretation of the references to color in this figure legend, the reader is referred to the web version of this article.)

avoided to simplify our analysis. In the following analysis, we primarily use splitting data averaged over each back azimuth swath provided by Christensen and Abers (2010), except in few occasions where individual splitting measurements from Hanna and Long (2012) are shown.

Fig. 3 displays observations at four representative stations, RC01 and TLKY close to the trench, HURN above the shallow wedge and WON above the deep wedge (Christensen and Abers, 2010; Hanna and Long, 2012). Available observations are primarily from three different back azimuths to the southeast ($\sim$105°–115°), southwest ($\sim$200°–210°) and northwest ($\sim$260°–290°). In general, the fast splitting direction observed at stations between the trench and the 50 km isodepth contour is sub-parallel to the absolute plate motion of the Pacific plate (e.g., station RC01, TLKY, Fig. 3a, b, e and f). At stations toward the northwest beyond the 100 km isodepth contour (e.g., station WON, Fig. 3d and h) the fast splitting direction is predominantly parallel or sub-parallel to the trench. In between these regions, the fast splitting direction varies strongly with the back azimuth of the incoming wave (e.g., station HURN, Fig. 3c and g). Although these rich and complicated splitting patterns are unexpected from the hexagonal symmetry with a dipping fast symmetry axis (or A-type fabric with a dipping symmetry axis), we will show in the next section that they can be a natural consequence of subducting asthenosphere.

3. Forward prediction of shear wave splitting

As done in Song and Kawakatsu (2012), we calculate splitting pattern by solving the Christoffel equation. The anisotropy parameter and elastic tensor used in this calculation are exactly the same as those given in the Supplementary Table S1 of Song and Kawakatsu (2012), which involves *P*-wave radial anisotropy of 4%, S-wave anisotropy of 3%, azimuthal anisotropy of 2% and the parameter η (Takeuchi and Saito, 1972) of 0.95. Such an elastic tensor with orthorhombic symmetry can be defined with a fast axis following the shear direction on the horizontal plane and a slow axis perpendicular to such a plane. Since the same splitting behavior can be reproduced with a suite of anisotropy model parameters that are consistent with previous seismic constraints on the oceanic asthenosphere (Supplementary Fig. S2 of Song and Kawakatsu, 2012), our discussion is focused on the reasoning and details of the predicted splitting pattern.

Since the direction of the fast axis in the oceanic asthenosphere is likely to align with the absolute motion of the Pacific plate, we first rotate the elastic tensor such that the fast axis aligns to the direction of the local plate motion obliquity α, which is defined as the acute angle between trench-normal and the plate motion direction (Fig. 2c). Considering a slab strike of 60°N (Rondenay et al., 2010) and global plate motion model NUVEl-1A (DeMets et al., 1994)

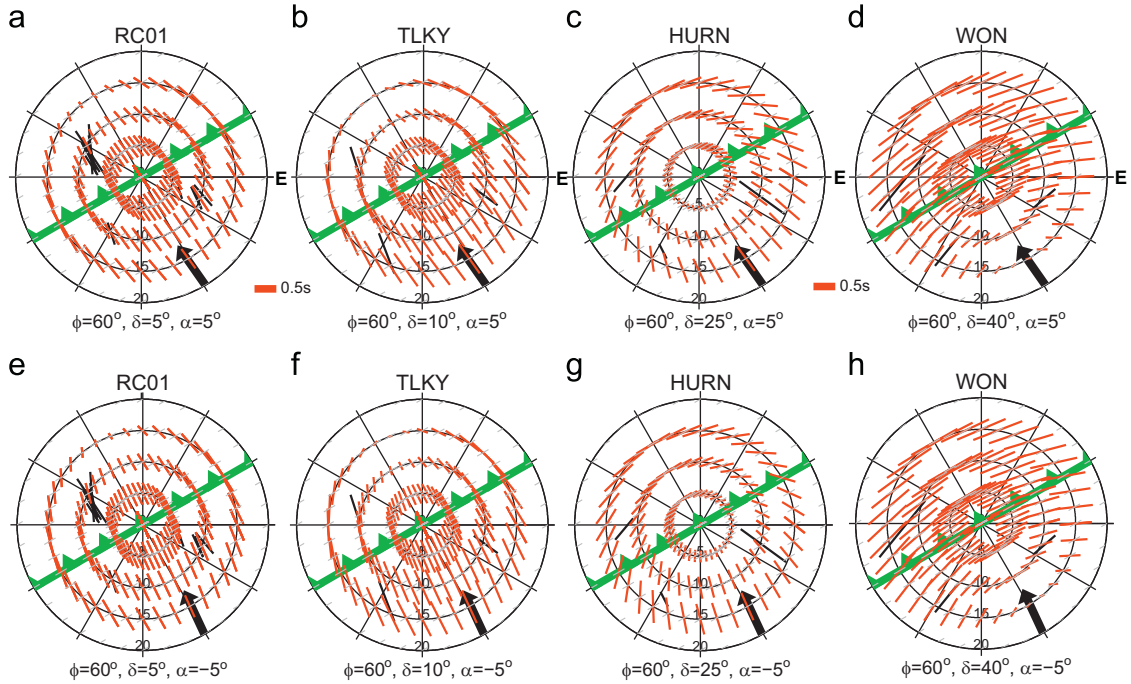

Fig. 3. Stereoplots display comparisons between observed and predicted splitting pattern in four representative stations in the fore-arc. (a) and (e) RC01. (b) and (f) TLKY. (c) and (g) HURN. (d) and (h) WON. Black bars display observations and red bars indicate synthetics shown every 10° in azimuth and every 5° in incident angle, while grey bars mark the strike of the trench for reference. The orientation of subduction is also represented as a thick green line with the triangles showing the direction of the dip and thick solid arrows indicate the plate motion direction. Strike ϕ, dip δ and plate motion obliquity α used in each calculation are indicated below each panel. (a)–(d) for α of 5°; (e)–(h) for α of $-5°$. (For interpretation of the references to color in this figure legend, the reader is referred to the web version of this article.)

under the Pacific hotspot reference frames HS3 (Gripp and Gordon, 2002), HS2 (Gripp and Gordon, 1990) and Atlantic hotspot reference frame (Kreemer, 2009), α is about $-5°$ to $+5°$. Subsequently, we rotate the elastic tensor with respect to the trench-axis by the slab dip δ (Fig. 2c). To facilitate a direct comparison between predictions and observations, we further rotate the elastic tensor within the horizontal plane such that the strike of the trench at 60°N is properly taken into account before solving the Christoffel equation to obtain the fast splitting direction at a given back azimuth and incident angle. The splitting time is then computed considering the difference between the fast and slow wave velocities with a constant layer thickness.

3.1. Fast splitting directions

Fig. 3a–d compare the predicted SKS splitting pattern with observations using the obliquity of 5° derived from the Atlantic hotspot reference frame and slab dips of 5°, 10°, 25° and 40°, respectively, mimicking the slab geometry across the fore-arc. For slab dips of 5° and 10°, the fast splitting pattern is dominated by the effect of the near-horizontal fast axis such that the predicted SKS fast splitting directions are consistently sub-parallel to the plate motion direction, independent of ray back azimuths (Fig. 3a and b). On the other hand, for a slab dip of 40°, the fast splitting pattern is dominated by the effect of the dipping slow axis (originally pointing vertical before subduction) such that the SKS fast splitting directions are always parallel or sub-parallel to the trench (i.e., typically within $\pm 10°$ from the strike of the trench) (Fig. 3d), independent of ray back azimuth. We also examine the splitting pattern using an obliquity of $-5°$ under the Pacific hotspot reference frame HS3 (Fig. 3e–h); however, the difference is quite small.

For a slab dip of 25°, there is a more sophisticated but systematic splitting pattern dictated by the competing effect of the tilted fast and slow axes. We can clearly observe a strong azimuthal dependence of fast splitting direction (Fig. 3c and g). The fast polarization direction changes from mostly parallel to the plate motion in the up-dip direction to trench-oblique along the strike of the trench, and to mostly trench-parallel in the down-dip direction. This behavior is not surprising given the difference in acute angle between the tilted axes and incoming waves from different directions (Song and Kawakatsu, 2012). Overall, these predictions are generally consistent with observed splitting directions within 10°.

3.2. Splitting times

One common notion on the prediction of splitting time is that it is directly proportional to the thickness of the anisotropy layer and the path length. Here, we wish to first highlight the effect of anisotropy symmetry alone on the splitting time (Figs. 3 and 4), $\delta t = (H \times (Vs_1 - Vs_2))/Vs_1 \times Vs_2$, where Vs_1 and Vs_2 are the phase velocity of the fast and slow S waves, respectively. Depending on the acute angle between rays and the tilted axis, the difference between Vs_1 and Vs_2 also varies (Fig. 4). For instance, at a slab dip of 10°, the predicted splitting time from the southeast and southwest back azimuths can be up to 40–50% larger than that from the northwest back azimuth when the incident angle is larger than 10° (Figs. 3a and 4a–c). For a slab dip of 40°, the opposite is true and the predicted splitting time from the northwest back azimuth is 40–50% larger than that from the southeast and southwest back azimuth (Figs. 3d and 4g–i). For a modest slab dip of 25°, the predicted splitting time does not change significantly as a function of back azimuth but strongly depends on the incident angle (Figs. 3c and 4d–f).

4. Hypothesis testing against the entire splitting dataset across the fore-arc

While we have shown that SKS splitting patterns predicted from the subduction of the asthenosphere agree quite well with

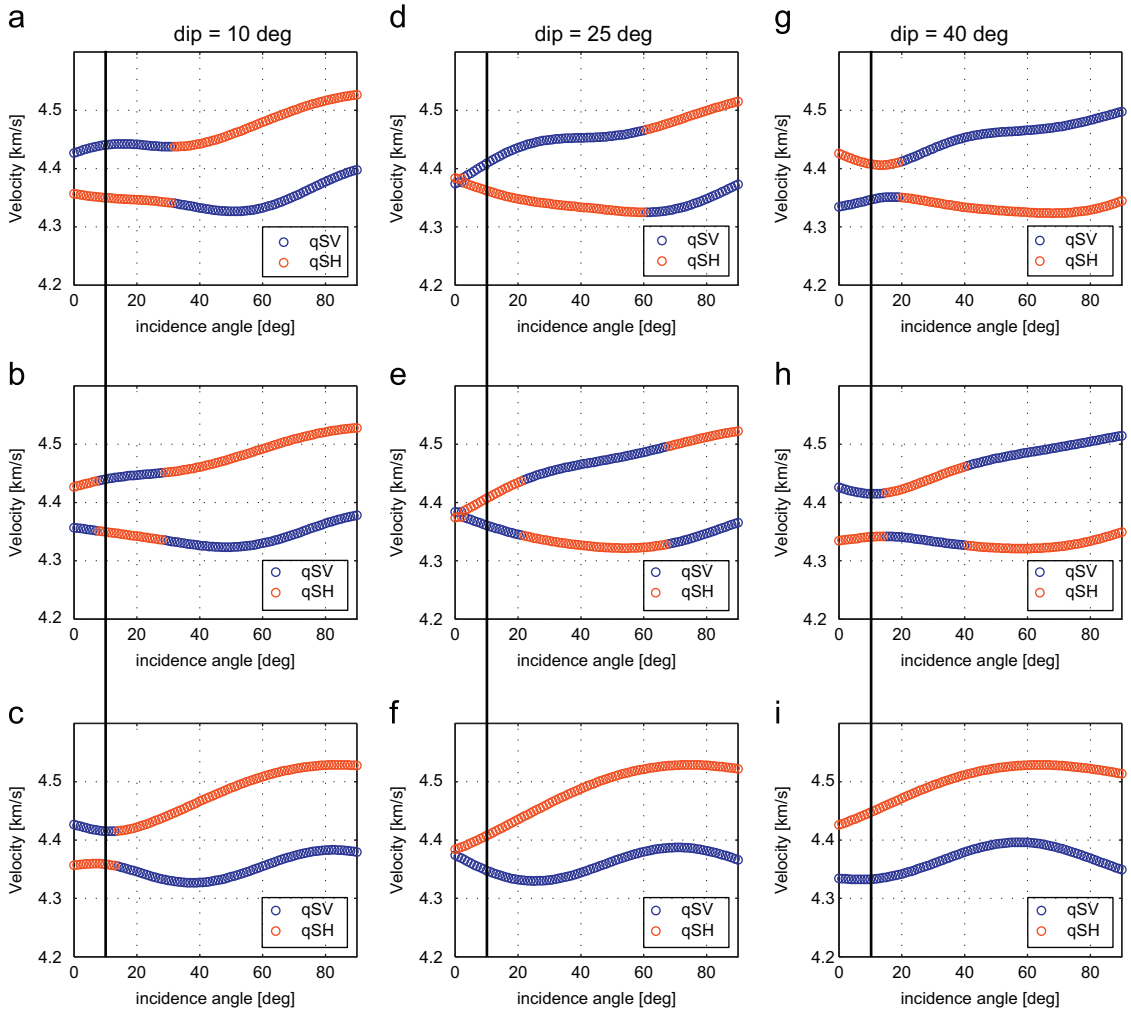

Fig. 4. Phase velocity of two quasi-S waves shown as a function of the incident angle for back azimuth swaths of southeast (SE) (a, d, and g), southwest (SW) (b, e and h) and northwest (NW) (c, f, and i), and slab dips of 10° (a, b, and c), 25° (d, e, and f) and 40° (g, h and i). Indicent angle of 10° is marked by the solid line for reference. Note that qSH wave is polarized sub-parallel to the trench strike for a near vertical incidence.

back-azimuthal variations in splitting direction at several representative stations, it is important to examine the entire splitting dataset (Christensen and Abers, 2010) against the scenario of subducting asthenosphere as well as other hypotheses. In this case, the splitting time is corrected for the path length at different back azimuth and incident angles using the simple geometric relationship as $L = H \times (1/\cos(\delta' \pm \theta))$, $\delta' = \tan^{-1}[\tan(\delta) \times \sin(\beta)]$, where L is the corrected path length; H is the layer thickness; θ is the incident angle; δ is the slab dip; δ' is the apparent dip along the direction of ray back azimuth; β is the angle between the strike of the trench and the ray back azimuth. $+$ $(-)$ operator applies when the ray is arriving from the down-dip (up-dip) direction. A layer thickness L of 250 km is chosen to be consistent with splitting times recorded at stations near the trench.

Furthermore, synthetic splitting patterns from two other models are included for comparisons. One is a hexagonal symmetry with a dipping fast axis normal to the trench, which we refer to as a model of "conventional slab entrainment". The other is a hexagonal symmetry with a horizontal fast axis parallel to the trench, which we refer to as a model of "trench-parallel flow". The strength of anisotropy is set at 1.5% for P waves and S waves with η of 0.95 in these cases. As discussed in the following section, examining the subducting asthenosphere model along with these two cases allow us to revisit the scenario of slab entrainment in a wider context and to discuss general prediction based upon large scale trench-parallel flow against observations in central Alaska.

Fig. 5 displays the entire splitting dataset of Christensen and Abers (2010) against predictions for a 250 km thick subducting asthenosphere (see also map view in Supplementary Fig. S1), dipping at about 15° near station TLKY, 22° near station HURN and beyond 30° near stations WON and SOB. In the northernmost 50 km of the array, we calculate splitting patterns considering a gentle slab geometry of 30°–35° (Abers et al., 2006) as well as a steep slab geometry of 40°–45° (Ratchkovski and Hansen, 2002; Rossi et al., 2006). We include calculations from SKS incident angles of 5°, 10° and 15° for different back azimuth swathes, southeast (105°–115°), southwest (200°–210°) and northwest (260°–290°), which allows us to examine the general trend as well as to illustrate the rich behavior associated with the subducting asthenosphere.

In the southeast swath, the synthetics display a general trend where the fast splitting direction changes from about $-30°$–40° to $-80°$ with increasing slab dip before jumping to about $+60°$–90° at a slab dip over 30° (Fig. 5a). This trend also appears in the observations. Note that the choice of different slab geometry in the northern end of the array does not make much difference in predicted splitting directions. One clear exception deviated from the general trend is MCK, which has a relatively small splitting

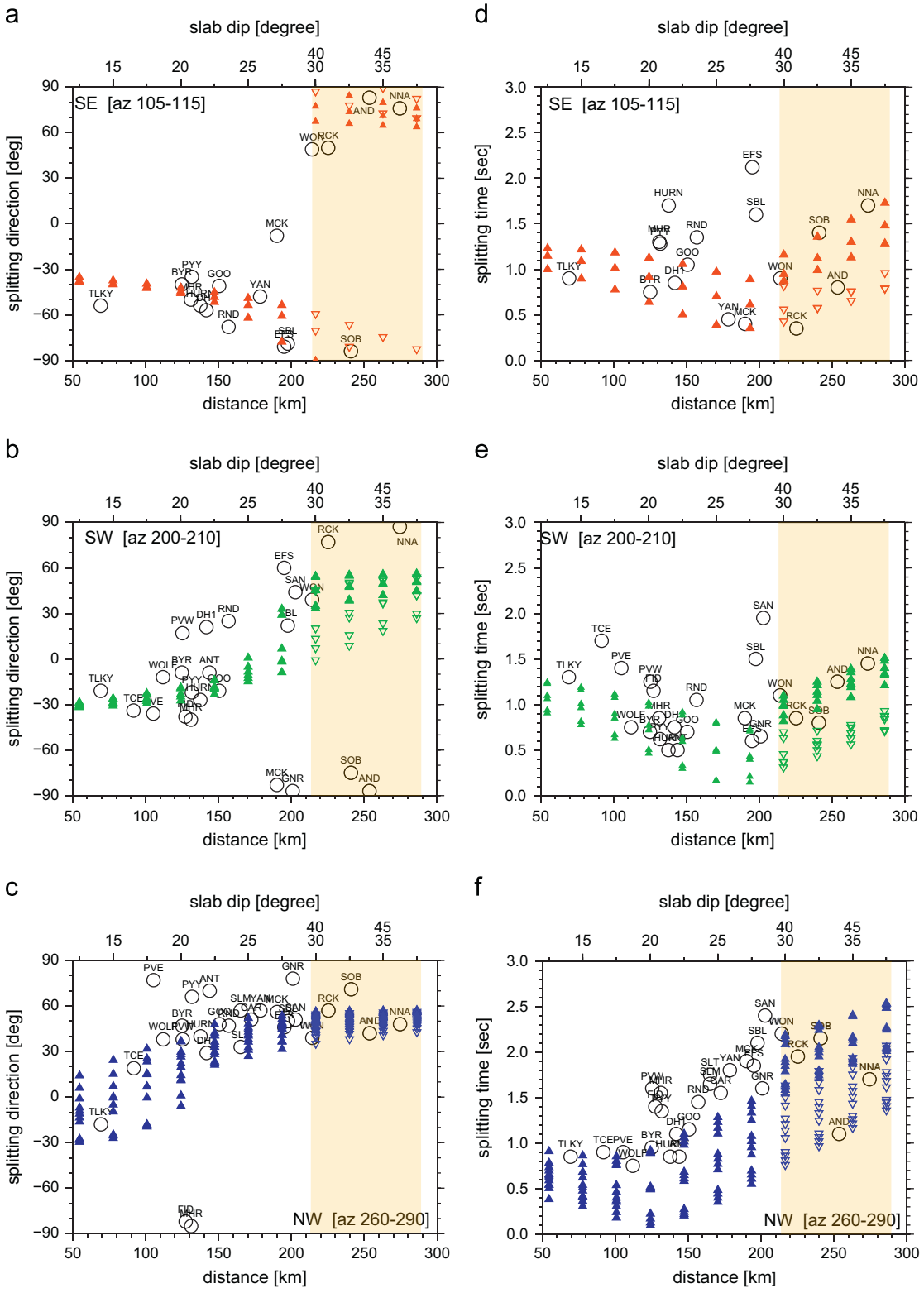

Fig. 5. Comparison between observed and predicted splitting patterns by the subducting asthenosphere across the entire fore-arc. Observations are projected along A–A′ profile (Fig. 1) and the predictions are plotted as a function of slab dip, mimicking increasing slab dip as the slab reaches deeper toward the northwest. (a), (b), and (c) display comparisons between observed (black open circles) and predicted (colored triangles) fast splitting directions in the southeast, southwest and northwest swathes, respectively. (d), (e), and (f) display comparisons between observed (black open circles) and predicted (colored triangles) splitting times in the southeast, southwest and northwest swathes, respectively. The synthetics are calculated every 10° in back azimuth, 2.5° in slab dip and incident angle of 5°, 10° and 15° in each backazimuth swath. Consequently, there are 3, 6 and 12 calculations included in southeast, southwest and northwest swath, respectively, for each slab dip. Shaded region marks the northern end of the array where calculations with a shallow slab dip (open inverse triangle) and a steep slab dip (solid triangle) are shown. (For interpretation of the references to color in this figure legend, the reader is referred to the web version of this article.)

time of less than 0.5 s. Otherwise, the difference between the predicted and observed splitting direction is typically less than 10°. As discussed previously, the predicted splitting times decrease to a minimum close to a slab dip of 25° partly due to the small difference in the phase velocities between the fast and slow waves (Fig. 4d), but they vary from 0.3 s at the slab dip of 25° to 1.7 s at the slab dip of about 45°. In general, the discrepancy in splitting time is not inconsistent with the splitting time estimated from the local S wave (Geoff Abers, personal communications), except in few instances such as EFS, HURN and SBL where the predicted splitting times are smaller than the observations by up to 1 s (Fig. 5d).

In the southwest swath, the synthetics display a general trend where the fast splitting direction remains at about −30° at a shallow slab dip (< 20°), and subsequently rotates clockwise linearly with the slab dip to about +40°–50° before stabilizing beyond a slab dip of

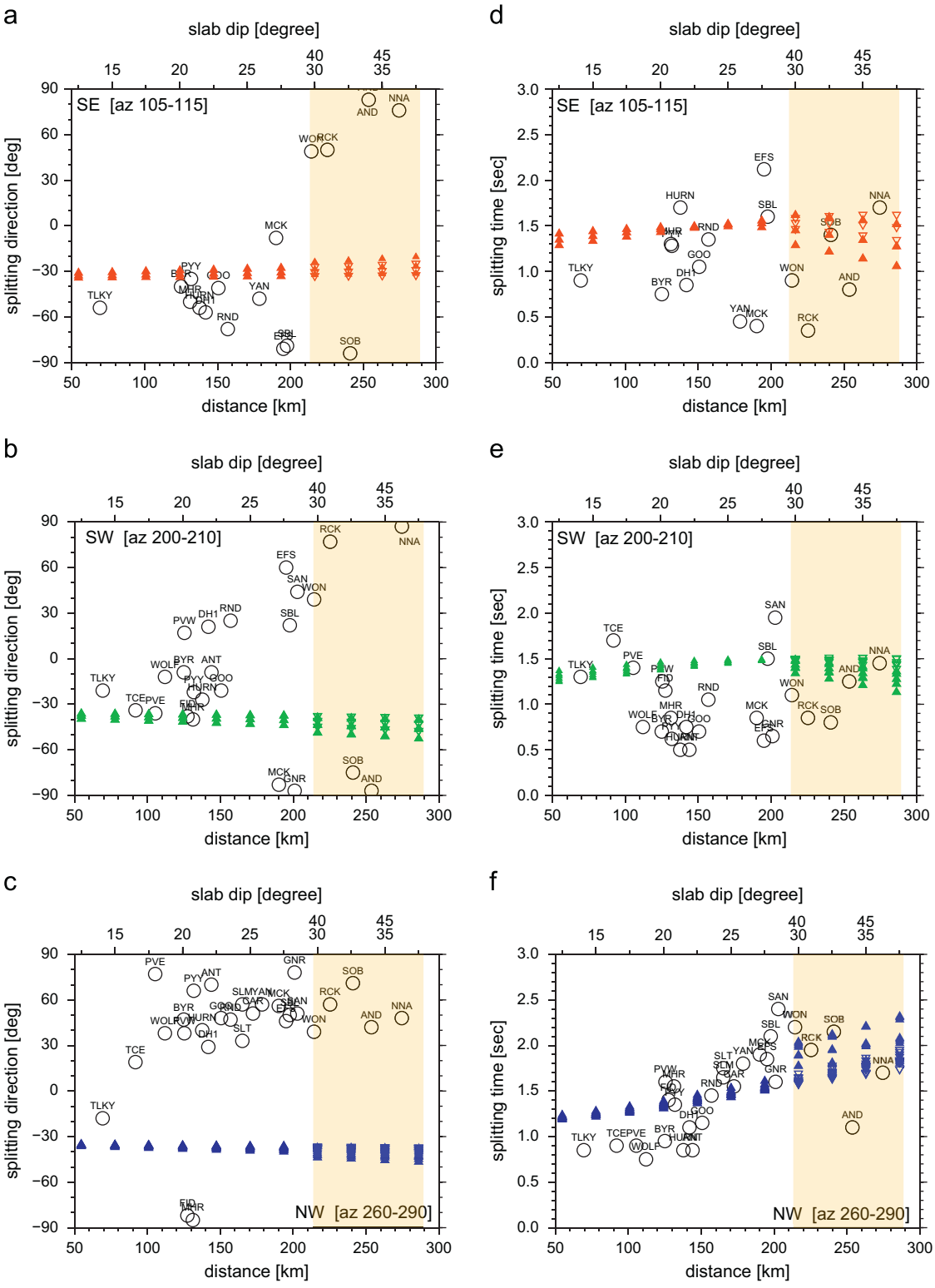

Fig. 6. Same as Fig. 5, except the predicted splitting pattern is calculated by "traditional slab entrainment" of a hexagonal symmetry with a tiled fast axis.

30–35° (Fig. 5b). Splitting directions predicted for different slab geometry in the northern end of the array differ by about 20° or less and they are frequently overlapped. The predicted trend also appears in the observations. Splitting directions from RND and DH1 in the northeastern part of the array and PVW in the westernmost part of the array appear off the trend, but they may be reconciled with a slightly higher dip angle close to 27.5°, as indicated in the seismicity profiles (Fig. 2a, Supplementary Fig. S2; Ratchkovski and Hansen, 2002). However, there are a few exceptions that are less well reconciled by predictions with any slab dip, including observations at stations MCK, AND, NNA, SOB, GNR and RCK. The splitting directions observed at these stations are between −80° and +70°, differing from predictions by up to 30°. We find that these stations appear spatially clustered near the northeast corner of the array and

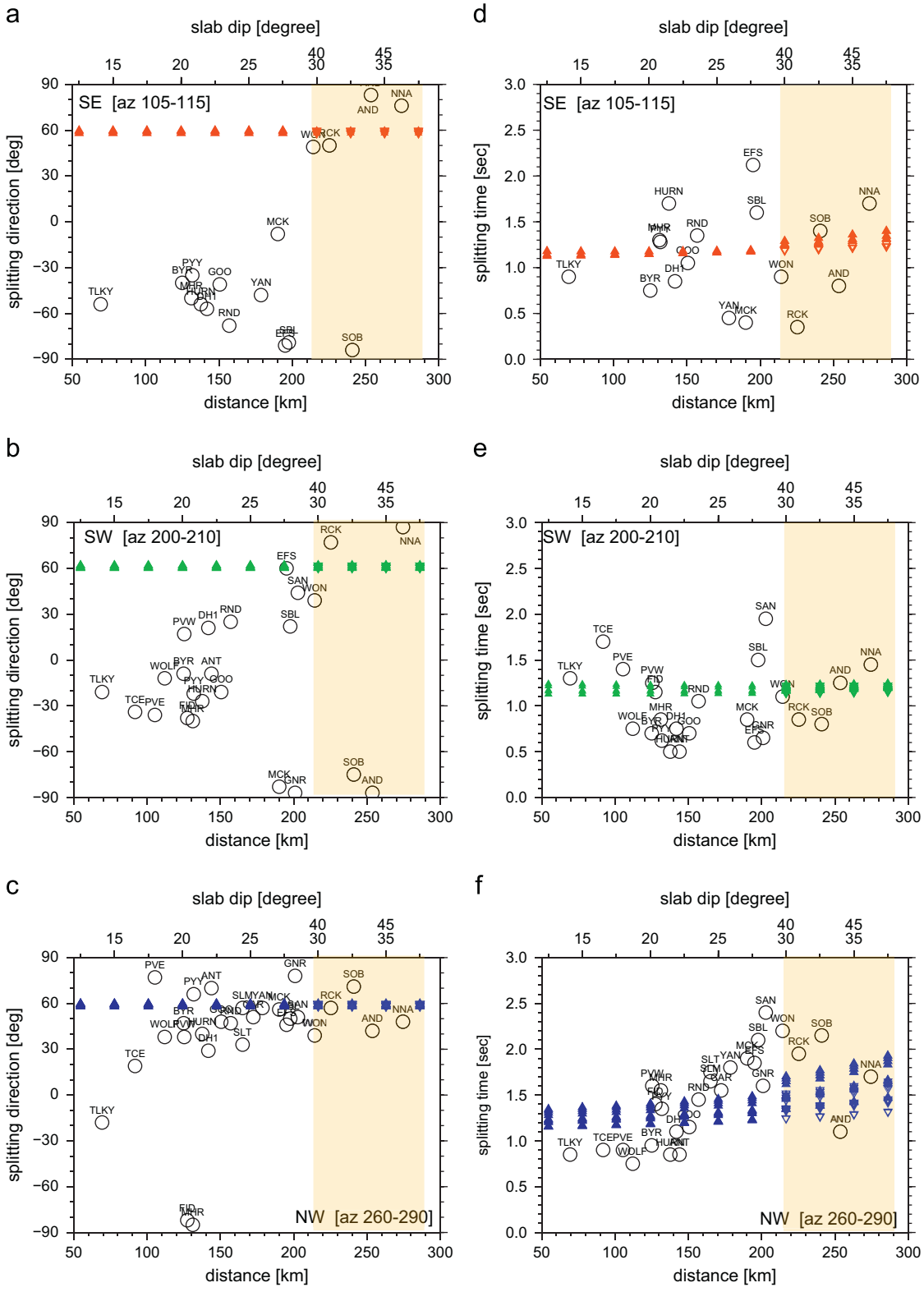

Fig. 7. Same as Fig. 5, except the predicted splitting pattern is calculated by "trench-parallel flow" of a hexagonal symmetry with a trench-parallel horizontal fast axis.

we will return to these outliers later in the discussion section. Similar to the southeast swath, the predicted splitting times decrease to a minimum at a slab dip of 25°, varying from 0.3 to 1.4 s (Fig. 5e).

In the northwest swath, the predicted splitting directions rotate from −30° to 20° linearly to +40° at a slab dip of 20°–25° before stabilizing at a larger slab dip (Fig. 5c). The choice of slab geometry in the northern end of the array does not make a noticeable difference in this swath. Several outliers previously identified in the southwest swath appear relatively close to the predicted splitting directions at slab dips over 20°. Since the northwest swath is the only azimuthal swath in the down-dip direction, the predicted splitting times are generally larger than those in the southeast and southwest swathes at a slab dip over 20° (Fig. 5f). The minimum of predicted splitting time is located at a relatively low dip angle of 20° and there is a linear increase beyond a slab dip of 20°, consistent with the unique trend identified in the observation.

It appears that, except a few outliers, the general splitting pattern as well as its down-dip variations at different back azimuths are generally well matched by the prediction despite that other sources of anisotropy either in the slab or the mantle wedge may exist. On the other hand, the model of conventional slab entrainment does satisfy observations near the trench, but it does not explain the observed splitting directions in the shallow wedge and deep wedge (Fig. 6). Similarly, the model of pure trench-parallel flow might accommodate observations in the deep wedge, but it is difficult to reconcile observations near the trench and shallow wedge (Fig. 7). One important point we attempt to make is that, unlike the model of subducting asthenosphere, the predicted splitting directions from the model of trench-parallel flow are very uniform. The predicted splitting direction from the model of traditional slab entrainment at any given slab dip is also limited to within 20° or less. For the model of pure trench-parallel flow, the predicted splitting direction is constant and independent of the ray back azimuth and the incident angle, which cannot account for most of the variations observed in the actual data. In a way, the hexagonal symmetry implemented in Figs. 6 and 7 is similar to the D-type olivine fabric (Karato et al., 2008). After testing *A*-type and *E*-type olivine fabrics for the conventional flow models, we find that neither one performs any better than the results shown in Figs. 6 and 7.

5. Discussions

We have shown that the subduction of the oceanic asthenosphere is capable of explaining the observed SKS splitting pattern across the entire fore-arc in central Alaska, supporting the scenario advocated by Song and Kawakatsu (2012) on the basis of a global dataset. Azimuthal variations in splitting directions further provide a powerful constraint on the anisotropy symmetry in the sub-slab mantle. The model predicts a switch of fast polarization direction from the quasi-SV wave (trench-normal) to the quasi-SH wave (trench-parallel) through the subducting asthenosphere and the change in the slab geometry, which dictates the competition between the effects of tilted slow and fast axes. Furthermore, subducting asthenosphere predicts relatively small splitting time ($\sim <0.5$–1 s) in the southeast and southwest back azimuth swathes, while reproducing the linear trend in splitting time that is only observed in the northwest swath. Despite that seismic anisotropy likely exists in the crust, wedge or/and the slab, subduction of oceanic asthenosphere appears to dominate the SKS splitting pattern across the entire fore-arc.

Although the estimate in the thickness of subducting asthenosphere ($\sim$250 km) is apparently higher than the global average of 100 ± 50 km (Song and Kawakatsu, 2012), it could be an overestimate since crust or/and slab/wedge anisotropy is not taken into account. Assuming that the wedge anisotropy contributes to splitting time of about 0.3 s, similar to the local S splitting measurement beneath the station WON (Hacker and Abers, 2012) and a number of measurements in the immediate vicinity to the west (Wiemer et al., 1999), the thickness of subducting asthenosphere is about 200 km. On the other hand, calculations with the plate motion obliquity α of −5° to 0° could yield an acceptable estimate of about 150–200 km since observations are relatively close to the point singularity (Crampin, 1991) where the difference between Vsh and Vsv is relatively small. Nevertheless, these estimates appear similar to other shallow subduction zones in Cascadia and Peru (Song and Kawakatsu, 2012).

While subducting asthenosphere is capable of explaining the majority of the splitting dataset, a few outliers in the southwest swath deserve to be discussed further (Fig. 5b). As discussed

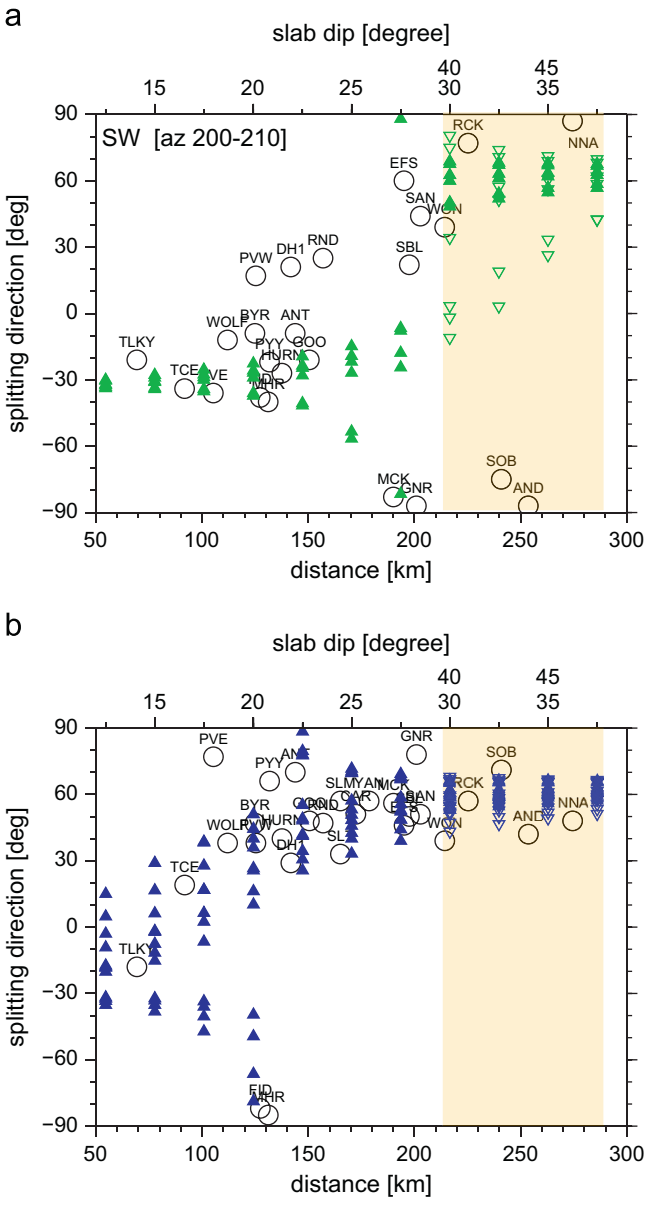

Fig. 8. Same as Fig. 5, except we only display comparisons of splitting directions in the southwest (a) and northwest (b) back azimuth swath where predictions display large variations in the slab dip of 20°–30° and match several outliers in the observations (see also maintext). The splitting direction is calculated with a slab strike ϕ of 70°N and plate motion obliquity α of 15°.

previously, some of these outliers are located near the northeastern part of the array (MCK, GNR, SOB, AND, RCK, NNA) (Fig. 1). Here we test a simple way to better reconcile these observations by looking at the effect of possible variations in the slab strike. We recomputed the splitting pattern using a strike of 70°N and consequently the plate motion obliquity of 15° (Fig. 8). While the predictions from this new setting are generally not very different from those shown in the southeast swath in previous calculations, the predictions for a slab dip of 25°–30°in the southwest swath display considerable changes that can reconcile with these outliers (Fig. 8a). Furthermore, two outliers in the northwest swath (e.g., FID, MHR) appear better explained (Fig. 8b). In the context of the subducting asthenosphere, it is clear that variations in slab strike can accommodate some of the observed complex splitting patterns. However, other possibilities such as anisotropy in the wedge/slab or crust deserve to be further explored.

5.1. Slab and wedge anisotropy

Previously, Christensen and Abers (2010) and Hanna and Long (2012) argued that the slab anisotropy or/and sub-slab entrainment as likely causes for the observations near the trench where the slab is sub-horizontal. If we consider a 2% azimuthal anisotropy constrained from global surface wave tomography (e.g., Smith et al., 2004; Debayle et al., 2005; Maggi et al., 2006) in the oceanic lithosphere, a slab thickness of about 65 km (Kumar and Kawakatsu, 2011) might accommodate splitting time of roughly 0.3 s, which is only a quarter to a third of the observed value near the trench (e.g., TLKY in Fig. 5). This estimate is certainly subject to better calibration with improved knowledge of anisotropy layering or/and variations in anisotropy strength/symmetry in the oceanic lithosphere (Song and Kim, 2012; Audet, 2013), but it seems to indicate a need for a substantial contribution of subducting asthenosphere to observations.

Typically, the effect of wedge anisotropy contributes to the splitting time of about 0.5 s or less in the fore-arc due to the relatively short path length and possibly complex fabrics in the wedge (e.g., Lassak et al., 2006; Levin et al., 2007; Wiens et al., 2008). Motivated by a linear increase in splitting time at stations above the mantle wedge in the northwest back azimuth, Christensen and Abers (2010) suggested that the mantle wedge anisotropy in central Alaska could be too strong to see slab or/and sub-slab anisotropy. They propose a two-layer model, arguing the presence of strong wedge anisotropy (~8%) with a trench-parallel fast axis in the top layer and a bottom layer with a trench-normal fast axis in the bottom layer. We found such a model reasonably explaining the splitting directions, but largely underestimating the splitting times (Supplementary Material and Supplementary Fig. S3). The possibility of trench-parallel fast direction or/and trench-parallel flow in the wedge is still viable (Mehl et al., 2003), and is suggested by recent 3D geodynamic models of Alaska (Jadamec and Billen, 2010, 2012). However, the trench-parallel flow predicted in the mantle wedge by numerical models is limited to toroidal flow around the slab edge. Thus, the results call upon comprehensive analysis on the wedge anisotropy symmetry along with realistic flow models in the future.

We, therefore, argue that subducting asthenosphere at least partly accounts for the linear increase in splitting times. In addition, it appears that seismic anisotropy in the mantle wedge does not seem to significantly affect the general SKS splitting pattern predicted by the subducting asthenosphere in central Alaska, particularly the splitting direction. We suggest that that the contribution of the mantle wedge anisotropy on SKS wave splitting data may be small either due to weak anisotropy or it is dictated by specific anisotropy symmetry (Ji et al., 2013). In either case, because the dominant period of local S waves is typically much shorter than the teleseismic SKS waves, the frequency dependence of splitting pattern due to wedge anisotropy shall be further investigated in the future.

5.2. Origin of the anisotropy in the sub-plate mantle

One of the most important conclusions in this validation work is that the anisotropy symmetry put forward by Song and Kawakatsu (2012) is probably representative of the oceanic asthenosphere and the sub-slab mantle, at least beneath the incoming Pacific plate and subducting slab in central Alaska. If this is the case, it is informative to compare it with those fabrics commonly used to infer mantle flow directions and to interpret SKS splitting observations: i.e., the A-type olivine fabric in the laboratory (Jung et al., 2006), average properties of natural samples from fast spreading ridges in the uppermost mantle (Ismail and Mainprice, 1998), and kimberlite nodules derived from the deep continental lithosphere (Ismail and Mainprice, 1998). To consider the effect of minor minerals such as orthopyroxene and clinopyroxene, we also include petrofabric data from xenoliths samples in two localities from western Canadian (Saruwatari et al., 2001), which are inferred to sample the deep lithosphere or the top of asthenosphere. While the fabrics of these natural samples do not necessarily represent the anisotropy symmetry in the oceanic asthenosphere since the scale of these samples (~ cms) is much smaller than the wavelength of seismic wave (~ tens of kilometers for 8 s SKS wave), they give a nice perspective on how the detailed anisotropy symmetry in nature may dictate the shear-wave splitting pattern.

Fig. 9 displays predicted phase velocities along the shear direction (or [100](010)) as a function of incident angle. We find that the *A*-type olivine and the average fabric of fast spreading ridges mimic the hexagonal symmetry with a horizontal fast axis where the quasi-SV wave is usually the fast wave except at a very high incident angle of at least 75°; there the fast wave changes from quasi-SV to quasi-SH wave and the fast polarization direction switches by 90° (Fig. 9b). On the other hand, the phase velocities of two quasi-S waves predicted by the average properties of kimberlite nodules has a crossover around 55°–60° (Fig. 9c). Samples from two localities of the western Canada indicate that the crossover takes place at even lower angles around 40° and 30° (Fig. 9d and e), respectively. In case of the recent high pressure and temperature experiment on olivine fabrics (Fig. 9f, Ohuchi et al., 2011), the crossover is even closer to the prediction by the inferred anisotropy symmetry in the oceanic asthenosphere (Fig. 9g).

It is worth noting that the anisotropy symmetry we infer in the oceanic asthenosphere and the sub-slab mantle is qualitatively analogous to the AG type olivine fabrics categorized by Mainprice (2007) (or previously defined as [010]-girdle type by Tommasi et al. (2000) and first discussed by Christensen and Crosson (1968)) even though it only accounts for about 10% of the entire petrofabric dataset. For the AG type olivine fabric, the concentration of olivine [010] axis is strong while [100] and [001] axes disperse along the (010) slip plane, which leads to orthorhombic symmetry with strong radial anisotropy and weak azimuthal anisotropy. However, we must point out that the detail splitting behavior from AG-type fabric can certainly vary, as clearly shown in Fig. 9c, d and e where the crossover of Vsv and Vsh occurs at different angles.

As discussed by Song and Kawakatsu (2012), several different mechanisms or processes such as the presence of small amount of oriented melt pockets (Holtzman et al., 2003), transpression (Tommasi et al., 1999) and the activation of dual slip systems [100](010) and [001](010) (Ohuchi et al., 2011) can come into play at the formation of [010]-girdle type fabrics. Although, the

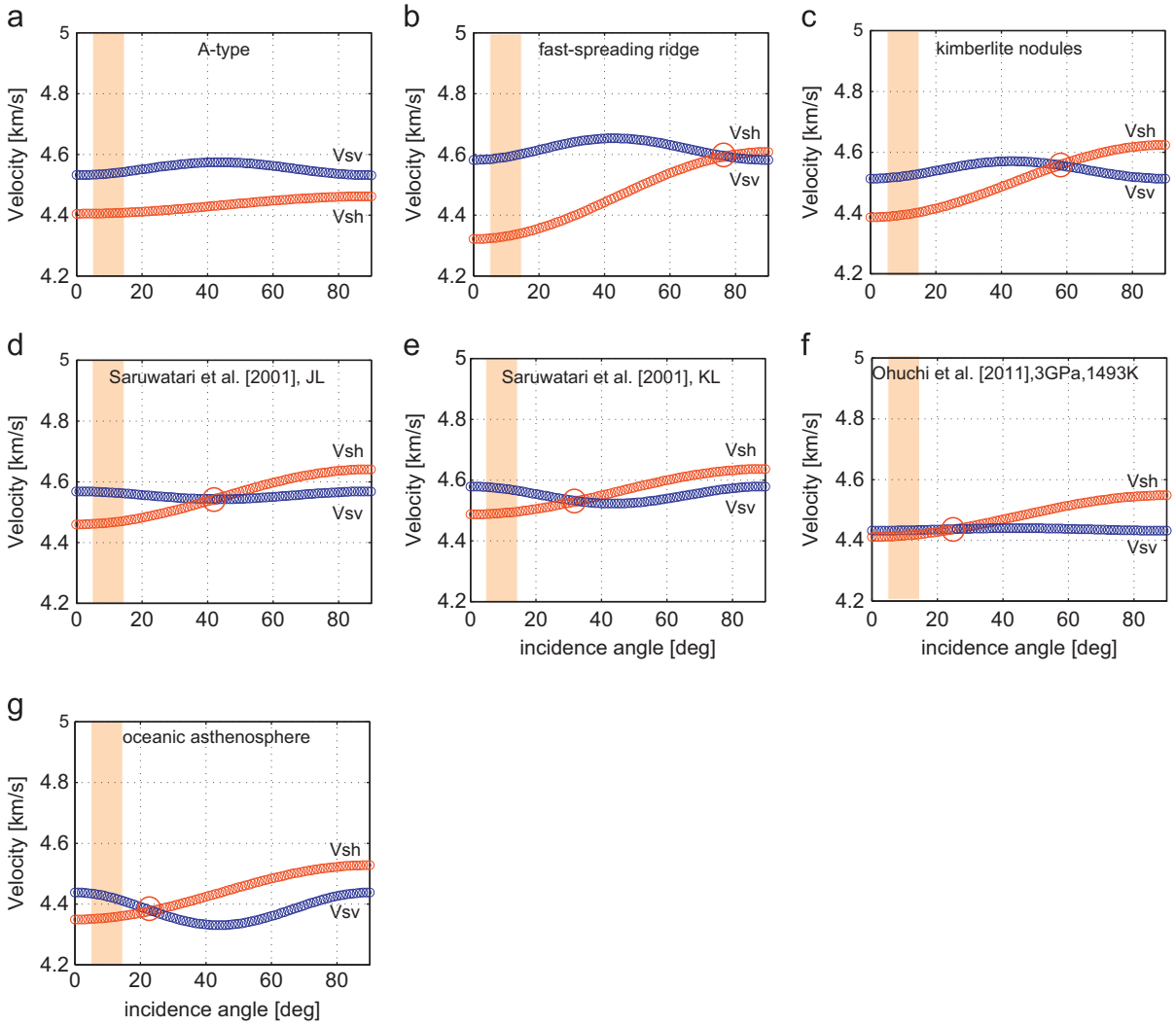

Fig. 9. Phase velocity along the shear direction (*a*-axis) of two quasi-S waves as a function of incident angle for the anisotropy symmetry observed in (a) A-type olivine (Jung et al., 2006), (b) average of fast spreading ridges (Ismail and Mainprice, 1998), (c) average of kimberlite nodules (Ismail and Mainprice, 1998), (d) and (e) mantle xenoliths at Jacques Lake (JL) and West Kettle River (KL) in western Canada (Saruwatari et al., 2001), (f) "A-type olivine" at 3 GPa, 1493 K (Ohuchi et al., 2011, see also Supplementary Fig. S4), (g) oceanic asthenosphere (Song and Kawakatsu, 2012) (inferred). The range of incident angle for SKS wave is marked in orange strip for reference and the location of the phase velocity crossover is marked by a red circle. (For interpretation of the references to color in this figure legend, the reader is referred to the web version of this article.)

effect of oriented melt pockets on radial anisotropy in the sub-slab mantle may diminish due to melt migration or/and solidification at depth, latest analysis indicates the development of olivine AG-type fabric due to melt-solid interaction (Higgie and Tommasi, 2012), which presumably has lasting effect on sub-slab anisotropy. Interestingly, the splitting patterns predicted by the olivine fabrics of Ohuchi et al. (2011) at asthenosphere pressure and temperature (Supplementary Fig. S4) resembles closely to the result of the subducting asthenosphere (Fig. 5) except the strength of anisotropy in the experiment is low (see also Fig. 9f), possibly due to the small shear strain on the sample (Ohuchi et al., 2011). Further evaluation of these various mechanisms on mantle fabrics will undoubtedly shed a new light on the linkage between tectonic processes and seismic anisotropy near deformation zones.

Processes and mechanisms that lead to the inferred anisotropy symmetry in the oceanic asthenosphere might be complex and subject to the nature of oceanic asthenosphere as well as its evolution history. By using near-vertical SKS waves, the detailed anisotropy property for many of the nature samples and oceanic asthenosphere are difficult to distinguish from each other and from the hexagonal symmetry with a horizontal fast axis, since the changes in the fast polarization direction only occur at higher angles ($>20^{\circ}$). One important point that we hope to elucidate in this paper is that, by taking advantage of the varying slab geometry either among different subduction zones (Song and Kawakatsu, 2012) or within a given subduction zone (this study), SKS waves sample sub-slab mantle over a wide range of angles from the tilted symmetry axis, presumably providing a much better constraint on the anisotropy symmetry in the sub-slab mantle.

5.3. Slab-mantle coupling and sub-slab flow

Even though the focus area is likely a few hundred kilometers away from the inferred slab edge (Eberhart-Phillips et al., 2006; Jadamec and Billen, 2010, 2012), our modeling result supports a dominant 2D slab entrainment flow pattern beneath the slab (e.g., Garfunkel et al., 1986; Ribe, 1992; Morishige and Honda, 2013) in spite of variations in along-strike variations in slab geometry. This conclusion is probably not unexpected as long as the oceanic asthenosphere is not decoupled from the slab. Since the degree

of toroidal flow component is intimately linked to the strength of the slab (Piromallo et al., 2006), mantle rheology and strain rate near the slab edge (Jadamec and Billen, 2010, 2012), our result implies that the scale of substantial 3D mantle flow (or toroidal component) beneath the slab may be less than a few hundred kilometers from the inferred slab edge. If this is the case, the length scale of the prominent toroidal flow ($\sim$100 s km) is much smaller than the length scale of the subducting plate ($\sim$1000 s km), as shown in a number of geodynamic calculations (e.g., Piromallo et al., 2006; Stegman et al., 2006; Kneller and van Keken, 2008; Honda, 2009; Morishige et al., 2010; Jadamec and Billen, 2012; Faccenda and Capitanio, 2013) as well as laboratory experiments (Kincaid and Griffins, 2003; Funiciello et al., 2004, 2006).

There are a few reasons potentially contributing to the dominance of the subducting asthenosphere in central Alaska and the lack of large-scale trench-parallel flow beneath the slab. Two ingredients essential to large-scale trench-parallel proposed in previous studies (Russo and Silver, 1994; Long and Silver, 2008, 2009) are the presence of a barrier at depth and slab rollback (or trench migration). We note that, in central Alaska, the interaction between the slab and the more viscous lower mantle could be relatively limited since the subduction is relatively shallow ($<$300 km depth). The trench migration rate is also very low in the area regardless of the mantle reference frame (e.g., Schellart et al., 2008). These conditions are probably unfavorable for large-scale trench-parallel flow. In any case, however, if the scenario of subducting asthenosphere applies globally as suggested by Song and Kawakatsu (2012) and this study, the asthenosphere is probably not decoupled from the subducting slab. Except in close proximity to a slab edge or rheological barrier (Jadamec and Billen, 2012; Faccenda and Capitanio, 2013; Miller and Becker, 2012), a 2D slab entrainment flow beneath the slab is expected to dominate near subduction zones around the globe.

Recent geodynamic modeling for subduction of a narrow plate emphasizes the importance of pure shear deformation near the slab edge due to large trench retreat (Faccenda and Capitanio, 2012; Buttles and Olson, 1998). In a way, such a strong pure shear beneath the slab can increase the strength of radial anisotropy (Tommasi et al., 1999), which is one of the essential ingredients in the subducting asthenosphere. However, such a conclusion may not apply to central Alaska with a large subducting plate (Faccenda and Capitanio, 2013). In addition, the absence of slab stagnation in the transition zone potentially limits the viability of this model to observations. Last but not the least, most geodynamic models implement CPO evolution based upon parameters suitable for a random initial fabric (Kaminski et al., 2004). However, if the initial CPO does have an impact on the evolution of olivine fabrics (Warren et al., 2008; Skemer et al., 2010), it is probably important to re-examine fabric evolution and preservation with respect to different type of initial CPO under different rheological conditions near the subducting slab.

6. Conclusion

We focus on back azimuth variations in splitting pattern to validate the scenario of subducting asthenosphere and investigate asthenospheric anisotropy. Complex observations of SKS splitting pattern in central Alaska can be grossly reproduced by the subduction of the oceanic asthenosphere after taking into account local slab geometry. Future effort will involve reconciliation of shear wave splitting measurements from seismic waves of different incident angles at a given subduction zone (e.g., SKS waves, teleseismic S wave) as well as the linkage between the subducting asthenosphere and the surface wave tomography of radial and azimuthal anisotropy near subduction zones, which shall provide additional constraint on the anisotropy symmetry beneath the slab and further evaluate the scenario put forward by Song and Kawakatsu (2012) and this report. Finally, the dominant contribution of the subducting asthenosphere on splitting pattern in subduction zones further invites a better understanding of the anisotropy property in the lithosphere, the subducting slab and mantle wedge, which remains to be resolved.

Acknowledgment

Discussions with A. Tommasi, D. Mainprice, F. Boudier, K. Higgie, G. Burrol, A. Vanchez, J.-P. Montanger, E. Kaminski, S. Chevrot, G. Abers, M. Fouch, C. Wolf, M. Faccenda and M. Morishige during the course of this work are greatly appreciated. M. Jadamec kindly provides thoughtful review on our manuscript and insights on 3D mantle flow in central Alaska. Y. Kim kindly provides latest result on slab geometry beneath central Alaska. We thank two anonymous reviewers for their constructive comments and criticisms, which improve and clarify our result. TAS greatly thanks support by D. Suetsugu at IFREE for the summer visit in U. Montpellier II in 2012. This study is supported by IFREE, JAMSTEC (TAS), and partly supported by Grant-in-Aid for Scientific Research 22000003 and 24654142 through JSPS.

Appendix A. Supplementary material

Supplementary data associated with this article can be found in the online version at http://dx.doi.org/10.1016/j.epsl.2013.02.010.

References

Abers, G.A., van Keken, P., Kneller, E.A., Ferris, A., Stachnik, J.C., 2006. The thermal structure of subduction zones constrained by seismic imaging: implications for slab dehydration and wedge flow. Earth Planet. Sci. Lett. 241, 387–397.
Ai, Y., Zhao, D., Gao, X., Xu, W., 2005. The crust and upper mantle discontinuity beneath Alaska inferred from receiver functions. Phys. Earth Planet. Inter. 150, 339–350.
Ando, M., Ishikawa, Y., Yamazaki, F., 1983. Shear wave polarization anisotropy in the upper mantle beneath Honshu, Japan. J. Geophys. Res. 88, 5850–5864.
Audet, P., 2013. Seismic anisotropy of subducting oceanic uppermost mantle from fossil spreading. Geophys. Res. Lett., 173–177.
Buttles, J., Olson, P., 1998. A laboratory model of subduction zone anisotropy. Earth Planet. Sci. Lett. 164, 245–262.
Christensen, N.I., Crosson, R.S., 1968. Seismic anisotropy in the upper mantle. Tectnophysics 6, 93–107.
Christensen, D.H., Abers, G., 2010. Seismic anisotropy under central Alaska from SKS splitting observations. J. Geophys. Res. 115, B04315.
Crampin, S., 1991. Effect of point singularities on shear-wave propagation in sedimentary basins. Geophys. J. Int. 107, 531–543.
Currie, C.A., Cassidy, J.F., Hyndman, R.F., Bostock, M.G., 2004. Shear wave anisotropy beneath the Cascadia subduction zone and western North America. Geophys. J. Int. 157, 341–353.
Debayle, E., Kennett, B., Priestley, K., 2005. Global azimuthal seismic anisotropy and the unique plate-motion deformation of Australia. Nature 433, 509–512.
DeMets, C., Gordon, R.G., Argus, D.F., Stein, S., 1994. Effects of recent revisions to the geomagnetic reversal time scale on estimates of current plate motion. Geophys. Res. Lett. 21, 2191–2194.
Eberhart-Phillips, D., Christensen, D.H., Brocher, T.M., Hansen, R., Ruppert, R.A., 2006. Imaging the transition from Aleutian subduction to Yakuta collision in central Alaska, with local earthquakes and active source data. J. Geophys. Res. 111, B11303.
Faccenda, M., Burlin, L., Gerya, T.V., Mainprice, D., 2008. Fault-induced seismic anisotropy by hydration in subducting oceanic plates. Nature 455, 1097–1110.
Faccenda, M., Capitanio, F.A., 2012. Development of mantle seismic anisotropy during subduction-induced 3-D flow. Geophys. Res. Lett. 39, L11305.
Faccenda, M., Capitanio, F.A., 2013. Seismic anisotropy around subduction zones: insights from three-dimensional modelling of upper mantle deformation and SKS splitting calculation. Geochem. Geophys. Geosyst. 14, 243–262.
Ferris, A., Abers, G.A., Christensen, D.H., Veenstra, E., 2003. High resolution image of the subducted Pacific (?) plate beneath central Alaska, 50–150 km depth. Earth Planet. Sci. Lett. 214, 575–588.
Fouch, M., Rondenay, S., 2006. Seismic anisotropy beneath stable continental interiors. Phys. Earth Planet. Inter. 158, 292–320.

Funiciello, F., Faccenna, C., Giardini, D., 2004. Role of lateral mantle flow in the evolution of subduction systems: insights from laboratory experiments. Geophys. J. Int. 157, 1391–1406.
Funiciello, F., Moroni, M., Piromallo, C., Faccenna, C., Cenedese, A., Bui, H.A., 2006. Mapping mantle flow during retreating subduction: laboratory models analyzed by feature tracking. J. Geophys. Res. 111, B03402.
Garfunkel, Z., Anderson, C.A., Schubert, G., 1986. Mantle circulation and the lateral migration of subducted slabs. J. Geophys. Res. 91, 7205–7223.
Gripp, A.E., Gordon, R.G., 1990. Current plate velocities relative to the hotspots incorporating the NUVEL-1 global plate motion model. Geophys. Res. Lett. 17, 1109–1112.
Gripp, A.E., Gordon, R.G., 2002. Young tracks of hotspots and current plate velocities. Geophys. J. Int. 150, 321–361.
Gung, Y., Panning, M., Romanowicz, B., 2003. Global anisotropy and the thickness of continent. Nature 442, 707–711.
Hacker, B.R., Abers, G.A., 2012. Subduction factory 5: Unusually low Poisson's ratio in subduction zones from elastic anisotropy of peridotite. J. Geophys. Res. 117, B06308.
Hanna, J., Long, M.D., 2012. SKS splitting beneath Alaska: regional variability and implications for subduction processes at a slab edge. Tectonophysics 530-531, 272–285.
Hayes, G.P., Wald, D.J., Lohnson, R.L., 2012. Slab 1.0: a three-dimensional model of global subduction geometries. J. Geophys. Res. 117, B01302.
Higgie, K., Tommasi, A., 2012. Feedbacks between deformation and melt distribution in the upper mantle: constraints from a microstructural study in the crust-mantle transition zone of the Oman ophiolite. Earth Planet. Sci. Lett. 359–360, 61–72.
Honda, S., 2009. Numerical simulations of mantle flow around slab edges. Earth Planet. Sci. Lett. 277, 112–122.
Holtzman, B.K., Kohlstedt, D., Zimmerman, M., Heidelbach, F., Hiraga, T., Hustoft, J., 2003. Melt segregation and strain partitioning: implications for seismic anisotropy and mantle flow. Science 301, 1227–1230.
Holtzman, B.K., Kendall, J.M., 2010. Organized melt, seismic anisotropy and plate boundary lubrication. Geochem. Geophys. Geosyst. 11, Q0AB06.
Ismail, W.B., Mainprice, D., 1998. A olivine fabric database: an overview of upper mantle fabrics and anisotropy. Tectonophysics 296, 145–157.
Jadamec, M.A., Billen, M.I., 2010. Reconciling surface plate motions with rapid three-dimensional mantle flow around a slab edge. Nature 465, 338–341.
Jadamec, M.A., Billen, M.I., 2012. The role of rheology and slab hinge on rapid mantle flow: three-dimensional numerical models of the Alaska slab edge. J. Geophys. Res. 117, B02304.
Ji, S., Li, A., Wang, Q., Long, C., Wang, H., Marcotte, D., Salisbury, M., 2013. Seismic velocities, anisotropy and shear-wave splitting of antigorite and tectonic implications for subduction zones. J. Geophys. Res. http://dx.doi.org/10.1002/grb.50110.
Jung, H., Katayama, I., Jian, Z., Hiraga, T., Karato, S., 2006. Effect of water and stress on the lattice-preferred orientation of olivine. Tectonophysics 421, 1–22.
Jung, H., Mo, W., Green, H.W., 2009. Upper mantle seismic anisotropy resulting from pressure-induced slip transition in olivine. Nat. Geosci. 2, 73–77.
Kaminski, E., Ribe, N.M., Browaeys, J.T., 2004. D-Rex, a program for calculation of seismic anisotropy due to crystal lattice preferred orientation in the convective upper mantle. Geophys. J. Int. 158, 744–752.
Karato, S.-I., Jung, H., Katayama, I., Skemer, P., 2008. Geodynamic signatures of seismic anisotropy of the upper mantle: new insights from laboratory studies. Annu. Rev. Earth Planet. Sci. 36, 59–95.
Kawakatsu, H., Kumar, P., Takei, Y., Shinohara, M., Kanazawa, T., Araki, E., Suyehiro, K., 2009. Seismic evidence for sharp lithosphere-asthenosphere boundaries of oceanic plates. Science 324, 499–502.
Kim, Y., Abers, G.A., Li, J., Christensen, D., Calkins, J., 2012. Imaging megathrust zone and Yukutat/Pacific plate interface in Alaska subduction zone. AGU Fall meeting abstract, San Francisco.
Kincaid, C., Griffins, R.W., 2003. Laboratory models of the thermal evolution of the mantle during rollback subduction. Nature 425, 58–62.
Kneller, E.A., van Keken, P.E., 2008. Effect of three-dimensional slab geometry on deformation in the mantle wedge: implications for shear wave anisotropy. Geochem. Geophys. Geosyst. 9, Q01003.
Kreemer, C., 2009. Absolute plate motions constrained by shear wave splitting orientations with implications for hotspot motions and mantle flow. J. Geophys. Res. 114, B10405.
Kumar, P., Kawakatsu, H., 2011. Imaging the seismic lithosphere-asthenosphere boundary of the oceanic plate. Geochem. Geophys. Geosyst. 12, Q01006.
Kustowski, B., Ekstrom, G., Dziewonski, A.M., 2008. Anisotropic shear-wave velocity structure of the Earth's mantle: A global model. J. Geophys. Res. 113, B06306.
Lassak, T.M., Fouch, M.J., Hall, C.E., Kaminski, E., 2006. Seismic characterization of mantle flow in subduction systems: can we resolve a hydrated mantle wedge? Earth Planet. Sci. Lett. 243, 632–649.
Lekic, V., Romanowize, B., 2011. Inferring upper-mantle structure by full waveform tomography with the spectral element method. Geophys. J. Int. 185, 799–831.
Levin, V., Okaya, D., Park, J., 2007. Shear wave birefringence in wedge-shaped anisotropic regions. Geophys. J. Int. 168, 275–286.
Long, M., Silver, P.G., 2008. The subduction zone flow field from seismic anisotropy: a global view. Science 319, 315–318.
Long, M., Silver, P.G., 2009. Mantle flow in subduction systems: the subslab flow field and implications for mantle dynamics. J. Geophys. Res. 114, B10312.
Maggi, A., Debayle, E., Priestley, K., Barruol, G., 2006. Azimuthal anisotropy of the Pacific region. Earth Planet. Sci. Lett. 250, 53–71.
Mainprice, D., Silver, P.G., 1993. Interpretations of SKS waves using samples from subcontinental lithosphere. Phys. Earth Planet. Inter. 78, 257–280.
Mainprice, D., 2007. Seismic anisotropy of the deep Earth from a mineral and rock physics perspectives. Treatise on Geophysics 2, 437–491.
Mehl, L., Hacker, B.R., Hirth, G., Kelemen, P.B., 2003. Arc-parallel flow within the mantle wedge: evidence from the accreted Talkeetna arc, south central Alaska. J. Geophys. Res. 108, 2375.
Miller, M.S., Becker, T.W., 2012. Mantle flow deflected by interactions between subducting slabs and cratonic keels. Nat. Geosci. 5, 726–730.
Montagner, J.P., Tanimoto, T., 1991. Global upper mantle tomography of seismic velocities and anisotropy. J. Geophys. Res. 96, 20337–20351.
Morishige, M., Honda, S., Tackley, P.J., 2010. Construction of semi-dynamic model of subduction zone with given plate kinematics in 3D sphere. Earth Planet Space 62, 665–673.
Morishige, M., Honda, S., 2013. Mantle flow and deformation of subducting slab at a plate junction. Earth Planet. Sci. Lett. 365, 132–142.
Nettles, M., Dziewonski, A.M., 2008. Radially anisotropic shear velocity structure of the upper mantle globally and beneath North America. J. Geophys. Res. 113, B02303.
Ohuchi, T., Kawazoe, T., Nishihara, Y., Nishiyama, N., Irifune, T., 2011. High pressure and temperature fabric transitions in olivine and variations in upper mantle seismic anisotropy. Earth Planet. Sci. Lett. 304, 55–63.
Panning, M., Romanowicz, B., 2006. A three-dimensional radially anisotropic model of shear velocity in the whole mantle. Geophys. J. Int. 167, 361–379.
Piromallo, C., Becker, T.W., Funiciello, F., Faccenda, C., 2006. Three-dimensional instantaneous mantle flow induced by subduction. Geophys. Res. Lett. 33, L08304.
Ratchkovski, N.A., Hansen, R.A., 2002. New evidence for segmentation of the Alaska subduction zone. Bull. Seismol. Soc. Am. 92, 1754–1765.
Ribe, M., 1992. On the relation between seismic anisotropy and finite strain. J. Geophys. Res 97, 8737–8747.
Rondenay, S., Montesi, L.G., Abers, G.A., 2010. New geophysical insight into the region of the Denali volcanic gap. Geophys. J. Int. 182, 613–620.
Rondenay, S., Abers, G.A., van Keken, P.E., 2008. Seismic imaging of subduction zone metamorphism. Geology 36, 275–278.
Rossi, G., Abers, G.A., Rondenay, S., Christensen, D.H., 2006. Unusual mantle Poisson's ratio, subduction, and crustal structure in central Alaska. J. Geophys. Res. 111, B09371.
Russo, R.M., Silver, P.G., 1994. Trench-parallel flow beneath the Nazca plate from seismic anisotropy. Science 263, 1105–1111.
Saruwatari, K., Ji, S., Long, C., Salisbury, M.H., 2001. Seismic anisotropy of mantle xenoliths and constraints on upper mantle structure beneath the southern Canadian Cordillera. Tectonophysics 339, 403–426.
Savage, M., 1999. Seismic anisotropy and mantle deformation: what have we learned from shear wave splitting. Rev. Geophys. 37, 65–106.
Schellart, W.P., Stegman, D.R., Freeman, J., 2008. Global trench migration velocities and slab migration induced upper mantle fluxes: constraints to find an Earth reference frame based on minimizing viscous dissipation. Earth Sci. Rev. 88, 118–144.
Silver, P.G., 1996. Seismic anisotropy beneath the continents: probing the depths and geology. Annu. Rev. Earth Planet. Sci. 24, 385–432.
Skemer, P., Warren, J., Kelemen, P., Hirth, G., 2010. Microstructural and rheological evolution of a mantle shear zone. J. Petrol. 51, 43–53.
Smith, D.B., Ritzwoller, M.H., Shapiro, N.M., 2004. Stratification of anisotropy in the Pacific upper mantle. J. Geophys. Res. 109, B11309.
Song, T.-R.A., Kawakatsu, H., 2012. Subduction of oceanic asthenosphere: evidence from sub-slab seismic anisotropy. Geophys. Res. Lett. 39, L17301.
Song, T.-R.A., Kim, Y., 2012. Anisotropic uppermost mantle in young subducting slab beneath central Mexico. Nat. Geosci. 5, 55–59.
Stegman, D.R., Freeman, J., Schellart, W.P., Moresi, L., May, D., 2006. Influence of trench width on subduction hinge retreat rates in 3-D models of slab rollback. Geochem. Geophys. Geosyst. 7, Q03012.
Takeuchi, H., Saito, M., 1972. Seismic surface waves. Methods in Computational Physics 11, 217–295.
Tommasi, A., Tikoff, B., Vauchze, A., 1999. Upper mantle tectonics: three dimensional deformation, olivine crystallographic fabrics and seismic properties. Earth Planet. Sci. Lett. 168, 173–186.
Tommasi, A., Mainprice, D., Canova, G., 2000. Viscoplastic self-consistent and equilibrium-based modelling olivine lattice preferred orientations: implications for the upper mantle seismic anisotropy. J. Geophys. Res. 105, 7893–7908.
Vinnik, L.P., Kosarev, G.L., Makeyeva, L.I., 1984. Anisotropy of the lithosphere from observations of SKS and SKKS. Dokl. Acad. Sci. USSR 278, 1335–1339. (in Russian).
Warren, J., Kelemen, P., Hirth, G., 2008. Evolution of olivine preferred orientation during simple shear in the mantle. Earth Planet. Sci. Lett. 272, 501–512.
Wiens, D.A., Conder, J.A., Faul, U.F., 2008. The seismic structure and dynamics of the mantle wedge. Annu. Rev. Earth Planet. Sci. 36, 421–455.
Wiemer, S., Tytgat, G., Wyss, M., Duenkel, U., 1999. Evidence for shear-wave anisotropy in the mantle wedge beneath south central Alaska. Bull. Seismol. Soc. Am. 89, 1313–1322.
Zhao, D., Christensen, D., Pulpan, H., 1995. Tomographic imaging of the Alaska subduction zone. J. Geophys. Res. 100, 6487–6504.